available at www.sciencedirect.com

ScienceDirect

journal homepage: www.elsevier.com/locate/chnjc

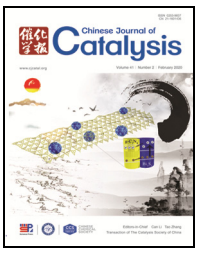

Article

# Enhanced low-temperature $NH_3$-SCR performance of $CeTiO_x$ catalyst via surface Mo modification

Lulu Li [a,c], Peixiao Li [d], Wei Tan [b], Kaili Ma [b], Weixin Zou [b], Changjin Tang [b,c,#], Lin Dong [a,c,*]

[a] *School of the Environment, Nanjing University, Nanjing 210093, Jiangsu, China*
[b] *School of Chemistry and Chemical Engineering, Nanjing University, Nanjing 210093, Jiangsu, China*
[c] *Jiangsu Key Laboratory of Vehicle Emissions Control, Center of Modern Analysis, Nanjing University, Nanjing 210093, Jiangsu, China*
[d] *Emergency Center for Environmental Monitoring at Canal Head of Middle Route of South-to-North Water Transfer Project, Nanyang 473061, Henan, China*

ARTICLE INFO

*Article history:*
Received 20 May 2019
Accepted 5 July 2019
Published 5 February 2020

*Keywords:*
$DeNO_x$
$CeO_2$-$TiO_2$ catalyst
$MoO_3$ modification
$SO_2$ poisoning
Surface acidity

ABSTRACT

The effect of molybdenum oxide on the activity and durability of $CeO_2$-$TiO_2$ catalyst for NO reduction by $NH_3$ was examined. It was found that the introduction of Mo could improve the low-temperature $NH_3$-SCR activity and $SO_2/H_2O$ durability of the $CeO_2$-$TiO_2$ catalyst and an optimal loading of Mo was 4 wt.%. The best $MoO_3/CeO_2$-$TiO_2$ catalyst displayed over 90% NO conversion from 200 °C to 400 °C and obtained 4-fold increase in NO conversion compared to $CeO_2$-$TiO_2$ at 150 °C. The characterization results revealed that the number of Brönsted acid sites over $MoO_3/CeO_2$-$TiO_2$ was significantly increased, and the adsorption of nitrate species was dramatically weakened because of the coverage of $MoO_3$, which were favorable for the high $NH_3$-SCR performance. It is believed that the $MoO_3/CeO_2$-$TiO_2$ catalyst is a suitable substitute for the $NH_3$-SCR reaction.



## 1. Introduction

Nitrogen oxides ($NO_x$) are major air pollution emission in industrial processes and human activities, which need to be tightly controlled under stringent environmental regulations. Selective catalytic reduction of NO with $NH_3$ ($NH_3$-SCR) over $V_2O_5$-$WO_3/TiO_2$ catalyst is an efficient and cost-effective technology for eliminating $NO_x$ from stationary sources [1–3]. This process, however, can be operated only in a rather high and narrow temperature range of 300–400 °C [4,5]. Unlike the case in a coal-fired power plant, the temperature of $NO_x$-containing exhaust gases from other sources such as glass furnace, metallurgy sintering furnace and cement plant is often lower than 300 °C [6–9]. Moreover, the biological toxicity caused by vanadium species also limits the application of vanadium-based $DeNO_x$ catalysts. Hence, the design of vanadium-free SCR catalysts that are sufficiently active at low temperature is highly desired.

In the past few years, Ce-based oxides emerged as a promising candidate for vanadium-based $NH_3$-SCR catalysts because of the high oxygen storage capacity (OSC) and facile $Ce^{4+}/Ce^{3+}$ redox cycle of $CeO_2$ [6,10–13]. Among them, Ce-Ti mixed oxide catalyst has drawn much attention because of its large surface area and good redox ability [14–16]. For instance, $CeO_2$-$TiO_2$

* Corresponding author. Tel: +86-25-83592290; Fax: +86-25-83317761; E-mail: donglin@nju.edu.cn
# Corresponding author. E-mail: tangcj@nju.edu.cn
This work was supported by the National Natural Science Foundation of China (21773106, 21707066, 21677069, and 21806077) and the China Postdoctoral Science Foundation (2018M642206).
DOI: S1872-2067(19)63437-6 | http://www.sciencedirect.com/science/journal/18722067 | Chin. J. Catal., Vol. 41, No. 2, February 2020

catalyst for $NH_3$-SCR reaction was first synthesized by Xu *et al.* [17] and admirable catalytic performance was observed at 275–400 °C. Afterwards, Gao *et al.* [18] explored the influence of preparation methods on the $NH_3$-SCR performance of $CeO_2$-$TiO_2$ catalyst and found that the catalyst prepared by single step sol-gel showed better SCR activity. However, the poor low-temperature SCR activity and $SO_2$ durability of these Ce-Ti-based catalysts still limit their practical application. Much effort to improve the low-temperature SCR catalytic performance of Ce-Ti-based catalysts has been made over the last several years. Among them, the introduction of other metal oxides to enhance their SCR activity has received considerable attention. The studies have proved that $CeO_2$-$TiO_2$ incorporated with various metals, such as Mn, W, Cu, Sn and Fe, achieved better $NH_3$-SCR catalytic performance [19–23]. $MoO_3$ was employed to increase the activity of traditional V-based de$NO_x$ catalyst [24]. Recently, Jiang *et al.* [25] prepared Ce-Mo-Ti oxide catalysts by a sol-gel method and found that the addition of Mo could improve the SCR activity of $CeO_2$-$TiO_2$ catalyst and its resistance to $SO_2$ and $H_2O$. Our study found that the incorporation of $MoO_3$ into $TiO_2$ could enhance the low-temperature activity and $SO_2$/$H_2O$ resistance of $CeO_2$/$TiO_2$ catalyst by improving the properties of carrier [26]. Li *et al.* [27,28] also revealed that the addition of $MoO_3$ has a promoting effect on the activity and arsenic resistance of supported $CeO_2$/$TiO_2$ catalyst. Nevertheless, few studies have focused on supported $MoO_3$/$CeTiO_x$ catalysts for $NH_3$-SCR reaction, which were obtained only by deposition of $MoO_3$ on $CeTiO_x$ support. Based on these findings, we considered that not only the supported $MoO_3$/$CeTiO_x$ could be a novel promising $NH_3$-SCR catalyst with high low-temperature activity and good durability of $H_2O$/$SO_2$, but also surface Mo modification alone is a good strategy to study the promoting effect of Mo on $CeTiO_x$ catalyst. Therefore, in this work, we attempted to develop a novel non-vanadium low-temperature $NH_3$-SCR catalyst by only loading $MoO_3$ on $CeTiO_x$ support. It was found that the addition of $MoO_3$ has a noticeable promoting effect on the activity of $CeO_2$-$TiO_2$ for the $NH_3$-SCR reaction. On the basis of the characterization results, the reason for the distinct promoting effect of $MoO_3$ has been elucidated.

## 2. Experimental

### 2.1. Catalyst preparation

$CeTiO_x$ mixed oxides with different Ce/Ti mole ratios (4:1, 1:1, 1:4) were prepared by an inverse co-precipitation method. In a typical synthesis, requisite amounts of ammonium cerium(IV) nitrate and titanium(IV) tetrachloride were dissolved in distilled water at room temperature and stirred for 1 h, and then the obtained slurry was added dropwise into excess ammonia (25%) under stirring until pH = 10. The milky solution was kept stirring for another 2 h, followed by aging for 24 h. The obtained precipitate was filtered and washed with deionized water until no pH change or $Cl^-$ residual (detected by the solution of $AgNO_3$) was detected. The obtained powder was dried at 110 °C overnight and then calcined in flowing air at 550 °C for 3 h. The $MoO_3$/$CeTiO_x$ catalysts were prepared by incipient-wetness impregnating the obtained $CeTiO_x$ supports with a proper amount of ammonium molybdate ($(NH_4)_6Mo_7O_{24}\cdot 4H_2O$) solution, then dried at 110 °C and calcined at 500 °C for 3 h. For simplicity, the obtained $MoO_3$/$CeTiO_x$ catalysts were denoted as *y*Mo/CT, where *y* is the mass fraction of the loaded Mo.

### 2.2. Catalyst characterization

Powder X-ray diffraction (XRD) was performed on a Shimadzu XRD-6000 power X-ray diffractometer with Cu $K_\alpha$ radiation ($\lambda$ = 1.5418 Å). The data were collected at $2\theta$ = 10°–80° with 8°/min scanning rate. Nitrogen adsorption-desorption isotherms were measured on a Micrometrics ASAP-2020 adsorption analyzer via the Brunauer-Emmett-Teller (BET) method at −196 °C. The samples (0.1 g) were activated for 4 h at 300 °C before each adsorption measurement. X-ray photoelectron spectroscopy (XPS) analysis was implemented on a PHI 5000 Versa Probe system at an accelerating power of 15 kW, equipped with monochromatic Al K (1486.6 eV) radiation. The adventitious C 1*s* peak at 284.6 eV was used as calibration to compensate the charging effect of the binding energies (BE, ± 0.1 eV error) of the samples. $H_2$-temperature-programmed reduction ($H_2$-TPR) was carried out using a $H_2$-Ar mixture (7 vol.% $H_2$) as reducing agent. Typically, 50 mg sample was used in a quartz U-tube reactor for each measurement. $NH_3$-temperature-programmed desorption ($NH_3$-TPD) experiments were performed on a multifunction chemisorption analyzer with a quartz U-tube reactor, detected by a thermal conductivity detector (TCD). Raman spectra were collected on a Spex 1877 D triplemate spectrograph with 2 $cm^{-1}$ resolution. A 532 nm DPSS diode-pump solid semiconductor laser was used as the excitation source with power output of ca. 5 mW. The *in situ* DRIFT spectra were collected on a Nicolet Nexus 5700 FTIR spectrometer with a scanning number of 32 at a resolution of 4 $cm^{-1}$, and a diffuse reflectance reaction cell (HARRICK) was used. For the experiments of $NH_3$ or NO + $O_2$ adsorption-desorption, the IR cell with sample was saturated with $NH_3$ (1 vol.%) or NO + $O_2$ (500 ppm NO and 5 vol.% $O_2$) for 1 h at room temperature, then the sample was purged with $N_2$ for 30 min, and the spectra were recorded at target temperature by raising the temperature from 50 °C to 400 °C.

### 2.3. Catalytic performance measurements

The activity tests were carried out on a fixed-bed quartz reactor using a 0.25 g catalyst of 40–60 mesh. The feed gas mixture contained 500 ppm NO, 500 ppm $NH_3$, 5% $O_2$, 6% $H_2O$ (when used), 200 ppm $SO_2$ (when used), and Ar as the balance gas. The total flow rate of the feed gas was 200 mL/min, corresponding to a GHSV of 48,000 mL $g^{-1}$ $h^{-1}$. The reaction temperature was increased from 100 to 400 °C. The composition of the gas in the inlet and outlet streams was measured with a quadrupole mass spectrometer (Dycor Dymaxion DM300M, AMETEK) when the catalytic reaction reached steady-state condition at each test temperature point.

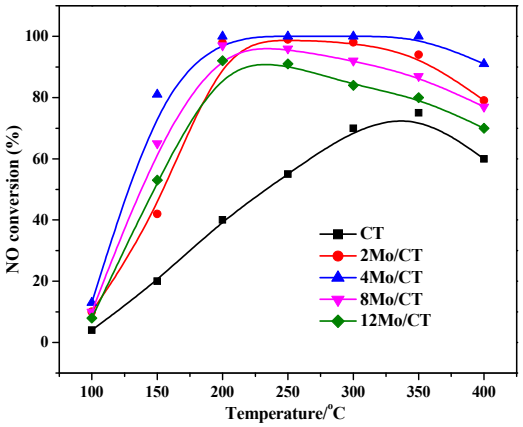


**Fig. 1.** NO conversions on these Mo/CT catalysts with different Mo contents and CT support.

## 3. Results and discussion

### 3.1. $NH_3$-SCR catalytic performance

#### 3.1.1. Effect of Ce/Ti mole ratio and Mo loading on catalytic activity over Mo/CT catalysts

First, a series of Mo/C*f*T samples with different Ce/Ti mole ratios (*f*) were prepared to explore the influence of Ce/Ti molar ratio on NO conversion over Mo/C*f*T catalysts. Herein, the loading amount of Mo was fixed at 4 wt.%. As shown in Fig. S1, the order of $NH_3$-SCR catalytic activity followed Mo/$Ce_4TiO_x$ > Mo/$Ce_1TiO_x$ > Mo/$Ce_{0.25}TiO_x$. The results of the catalytic activities indicated that Mo/$CeTiO_x$ catalyst exhibited the optimal NO conversion when the molar ratio of Ce/Ti was 4:1. Then, a series of *y*Mo/$Ce_4TiO_x$ samples with different Mo loadings were prepared and the $NH_3$-SCR activity was tested. As shown in Fig. 1, activity test results showed that the pristine $Ce_4TiO_x$ support had rather poor SCR activity in the whole operation temperature range (100–400 °C) with the maximum NO conversion of 71% at 350 °C. In contrast, the *y*Mo/$Ce_4TiO_x$ catalysts displayed much higher SCR activity in the temperature range of 200–400 °C. Among which, 4Mo/$Ce_4TiO_x$ sample exhibited a NO conversion of more than 90% within a broad operation temperature window (200–400 °C) under the GHSV of 48000 mL $g^{-1}$ $h^{-1}$. Most notably, the addition of Mo significantly increased the activity of $Ce_4TiO_x$ catalyst in the low-temperature range, obtaining 4-fold increase in NO conversion compared to $Ce_4TiO_x$ at 150 °C (from *ca.* 20% to *ca.* 80%). These results indicated that loading Mo on $Ce_4TiO_x$ surface had a remarkable promoting effect on $NH_3$-SCR activity especially at low temperature and the optimal loading amount was 4 wt.% Mo. Therefore, comparative studies between 4Mo/$Ce_4TiO_x$ catalyst (Mo/CT for short in the following chapters) and $Ce_4TiO_x$ support (CT for short) were conducted to elucidate the effect of $MoO_3$ loading on $NH_3$-SCR performance.

#### 3.1.2. Influence of $SO_2$ and $H_2O$ on the $NH_3$-SCR activity over CT and Mo/CT

The existence of sulfur dioxide and water vapor was unavoidable in the industrial application of $NH_3$-SCR catalysts, so it is important to evaluate the influence of $SO_2$ and water on the catalytic performance of our de$NO_x$ catalyst. Thus, the $SO_2$ and $H_2O$ resistance of the Mo/CT catalyst during $NH_3$-SCR reaction at 250 °C was evaluated through a long-time test, and the corresponding results are presented in Fig. 2. When 200 ppm $SO_2$ was injected at 250 °C (Fig. 2A), the NO conversion of the Mo/CT catalyst decreased slightly at first and then was kept at about 94% during the test period. Meanwhile, the $NH_3$-SCR activity of the CT sample was also measured in the presence of 200 ppm $SO_2$ as a comparison. The results showed that the NO conversion over CT slowly decreased with an increase in time and was kept at *ca.* 40% after 24 h. Moreover, when 200 ppm $SO_2$ and 5 vol% $H_2O$ were introduced into the reaction gas at the same time (Fig. 2B), the deactivation of the CT sample was much faster than that of Mo/CT. After 24 h, the NO conversion on the CT sample decreased from *ca.* 56% to *ca.* 29%, and the decline rate of the activity was 27%. However, the NO conversion over the Mo/CT sample still maintained at about 92%. The above results indicated that the Mo/CT catalyst exhibited above 90% NO conversion in the range of 200–400 °C and good $H_2O/SO_2$ resistance at 250 °C for $NH_3$-SCR reaction. Therefore, the Mo/CT catalyst can be used to remove $NO_x$ from stationary

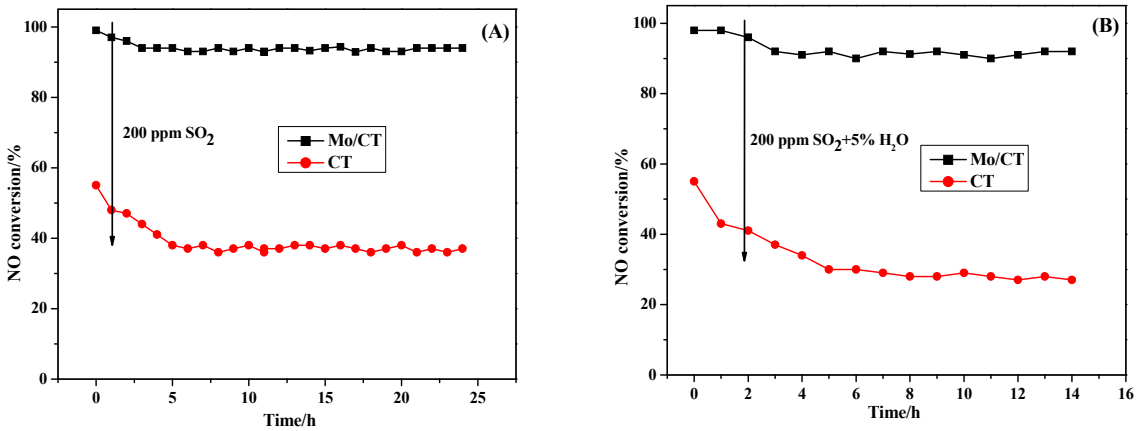


**Fig. 2.** $SO_2$ (a) and $H_2O+SO_2$ (b) resistance of the CT and Mo/CT catalysts at 250 °C.

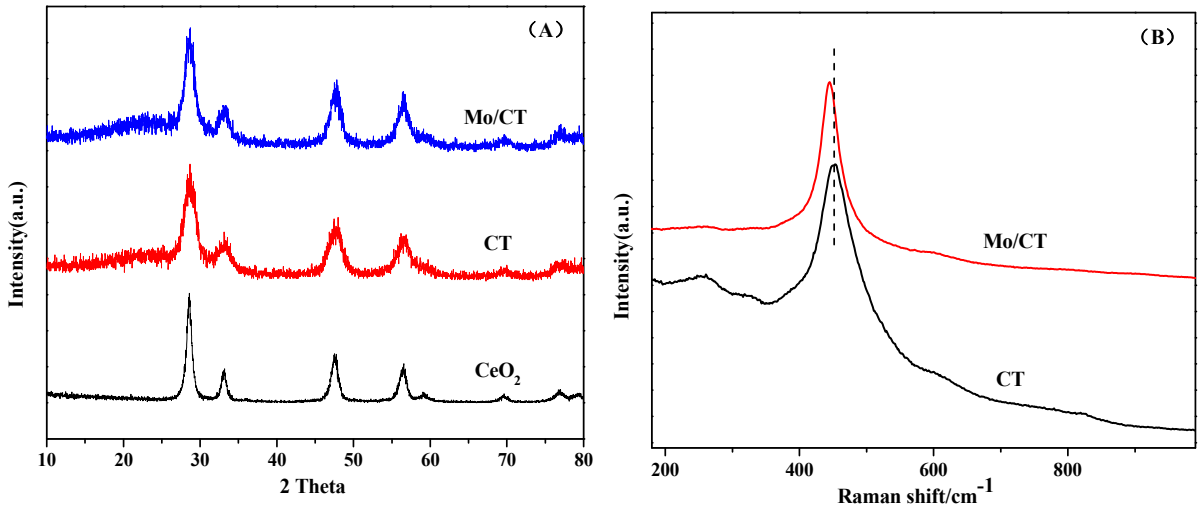


**Fig. 3.** XRD (A) and Raman (B) patterns of the CT and Mo/CT samples.

pollution sources containing a certain amount of $SO_2$ and $H_2O$ vapor because of its great catalytic performance.

### 3.2. Catalyst characterization

#### 3.2.1. Structural and textural characteristics (XRD, Raman and BET)

Fig. 3A presents the XRD patterns of CT and Mo/CT catalysts. Both samples exhibited the fluorite type crystalline structure without any phase segregation, characteristics of $CeO_2$ (PDF-ICDD 34-0394) [29]. Furthermore, no diffraction peak attributed to $MoO_3$ was detected in the XRD pattern of Mo/CT catalyst, which indicated that the molybdenum oxide was highly dispersed or presented as amorphous entities on the surface of CT [30]. To get further information of Mo species, Raman characterization was operated. It is well known that in comparison with XRD, Raman is more sensitive to distinguish the dispersion state of Mo. Fig. 3B displays Raman spectra of CT and Mo/CT samples. It shows that the two Raman spectra all exhibited a main band ascribed to the triply degenerate $F_{2g}$ mode of fluorite ceria and no Raman bands corresponding to $MoO_3$ were detected, indicating that $MoO_3$ was indeed present in the form of highly dispersed state on the surface of the CT support [31,32]. Moreover, the Raman band intensity of the Mo/CT catalyst was weaker than that of the CT support, which also suggested that the highly dispersed $MoO_3$ species on the surface of CT covered the support and weakened the signal [33]. These Raman results are in good agreement with XRD. We also noted that the $F_{2g}$ band of the Mo/CT catalyst shifted slightly from 451 to 444 $cm^{-1}$ owing to electronic interactions between $MoO_3$ and CT support.

$N_2$ adsorption/desorption isotherms of the samples were collected to understand the textural properties of CT and Mo/CT. It can be observed from Fig. 4A that both samples exibit type-IV isotherms according to IUPAC classification, showing the presence of mesoporous structure [34]. Besides, the H3-type hysteresis loops ($P/P_0$ of 0.4–1.0) manifested the presence of irregular pores, which was revealed by the BJH pore distribution curves (Fig. 4B). Table 1 shows BET surface area and pore structure results of the two catalysts. The specific surface area and total pore volume of CT was 135 $m^2/g$ and 0.303 $cm^3/g$, while that of Mo/CT was 101 $m^2/g$ and 0.273 $cm^3/g$, respectively. The specific surface area and total pore volume of Mo/CT decreased owing to the blocking effect of the CT support by the deposited molybdenum oxide. However, the $A_{BET}$ values of CT and Mo/CT followed the opposite trend of the corresponding SCR activity. Therefore, we believe that the improvement of the SCR activity over Mo/CT catalyst cannot be attributed to the changes of specific surface area caused by

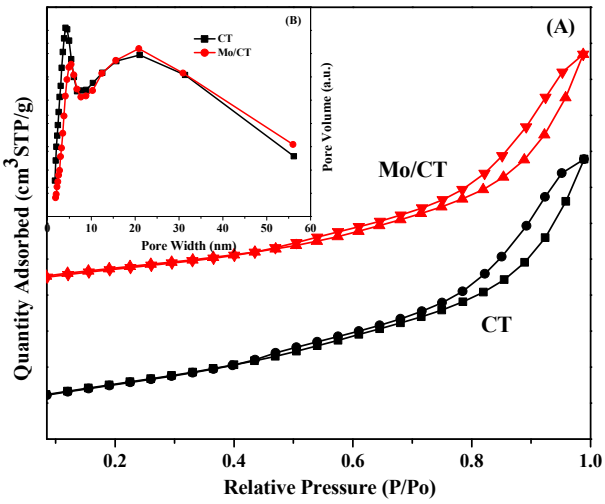


**Fig. 4.** $N_2$ adsorption/desorption isotherms of the CT and Mo/CT samples (inset is BJH pore distribution curves).

**Table 1**
The results of BET, XPS, and $NH_3$-TPD.

| Sample | BET specific surface area ($m^2/g$) | Total pore volume ($cm^3/g$) | Atomic ratio (%) | Acidity (mg/g) |
|---|---|---|---|---|
| CT | 135 | 0.303 | 49.2 | 0.49 |
| Mo/CT | 101 | 0.273 | 33.1 | 0.68 |

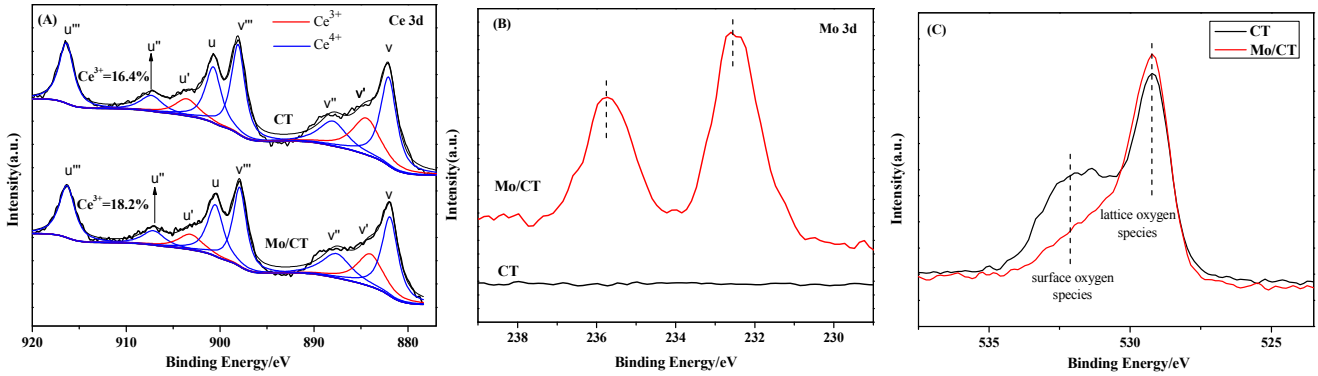


**Fig. 5.** XPS spectra of Ce 3*d* (A), Mo 3*d* (B) and O 1*s* (C).

molybdenum addition.

### 3.2.2. *Surface chemical states analysis (XPS)*

XPS experiments were conducted to explore the chemical states of surface species and the types of oxygen species over CT and Mo/CT samples, as presented in Fig. 5. For the Ce 3*d* XPS spectra in Fig. 5A, the bands labeled μ, μ', μ'', ν, ν' and ν'' represented the $3d^{10}4f^0$ state of $Ce^{4+}$, whereas u' and v' represented the $3d^{10}4f^1$ state, corresponding to $Ce^{3+}$ [6,14]. It can be seen that the redox pair of $Ce^{3+}/Ce^{4+}$ was observed in the Mo/CT and CT catalysts. According to the area ratio of the peaks representing $Ce^{3+}$ and $Ce^{4+}$, the percentage of $Ce^{3+}$ in the total Ce ($Ce^{3+}$ and $Ce^{4+}$) could be calculated. The addition of molybdenum to CT led to the slight increase in the percentage of $Ce^{3+}/(Ce^{3+} + Ce^{4+})$, which indicated there was interaction between the oxides of Mo and Ce. With regard to Mo 3*d* XPS spectra in Fig. 5B, two main peaks owing to Mo $3d_{5/2}$ and Mo $3d_{3/2}$ were observed at 232.2 and 235.6 eV, which were attributed to $MoO_3$ or $Mo^{6+}$ oxide [35,36]. The O 1*s* XPS information of these samples was presented in Fig. 5C. The peak at 532.1 eV was considered as surface oxygen species (donated as $O_\alpha$), and the band of $O_\beta$ at 529.2 eV was ascribed to lattice oxygen species. The $O_\alpha/(O_\alpha + O_\beta)$ ratio of all the samples were calculated by the area integral of $O_\alpha$ and $O_\beta$. It was found that the relative concentration ratio of $O_\alpha$ over Mo/CT catalyst was lower than that of CT (Table 1), suggesting that the number of surface oxygen species decreased after the introduction of molybdenum.

### 3.2.3. *Redox properties*

The redox properties of an $NH_3$-SCR catalyst always play an important role in the $NH_3$-SCR catalytic performance [37–39]. Thus, $H_2$-TPR was carried out to evaluate the redox properties of CT and Mo/CT catalysts. As shown in Fig. 6, three reduction peaks were observed for the two samples, which were assigned to the reduction of the surface oxygen species of ceria (α), the reduction of surface $Ce^{4+}$ (β), and the reduction of bulk of $Ce^{4+}$ (γ), respectively [29,40,41]. In addition, the reduction of the well dispersed Mo species and surface $Ti^{4+}$ was also likely to be included in peak β [28]. It is worth noting that loading Mo could slightly affect the reduction temperature for peak β. The β peak moved to higher temperature, from 570 °C for CT to 582 °C for Mo/CT, which was caused by the coverage of molybdenum oxides. Similar results were also obtained for vanadium and tungsten dispersed on $CeO_2$ [42]. At the same time, the area of peak α over the Mo/CT sample attributed to the reduction of surface oxygen species obviously declined because of the loading of Mo. This phenomenon illustrated that Mo loaded on CT could decrease the number of labile surface oxygen and defect sites, leading to low reducibility of the catalysts. This deduction can be supported by the results of XPS spectra shown in Fig. 5. It is clear that the $O_\alpha$ signal representing surface chemisorbed oxygen was much higher for CT than for Mo/CT. These results were also in line with the observations of Li *et al.* [35]. In brief, the $H_2$-TPR result manifested that the reducibility of Mo/CT was restrained compared with CT. According to the above characterization results and $NH_3$-SCR activity in Fig. 1, the experiments of $NH_3$-TPD and *in situ* DRIFTS were carried out to explore the reason for better catalytic activity of Mo/CT. The results may be more relevant for assessing the catalytic performance of the $NH_3$-SCR catalysts because they were obtained under conditions very close to or even identical with those of the catalytic reaction.

## 3.3. *Adsorption properties*

### 3.3.1. *$NH_3$-TPD*

Surface acid properties of $NH_3$-SCR catalysts are another

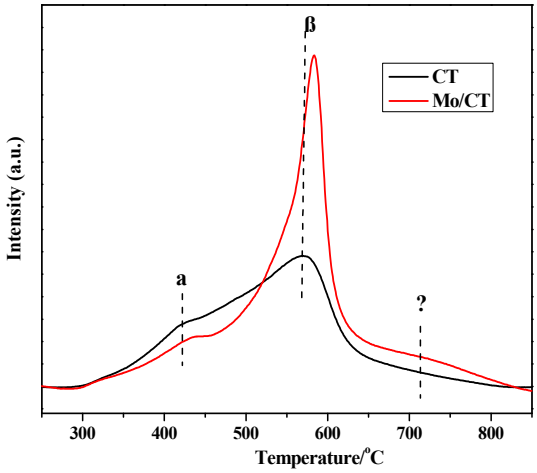


**Fig. 6.** $H_2$-TPR profiles of the CT and Mo/CT samples.

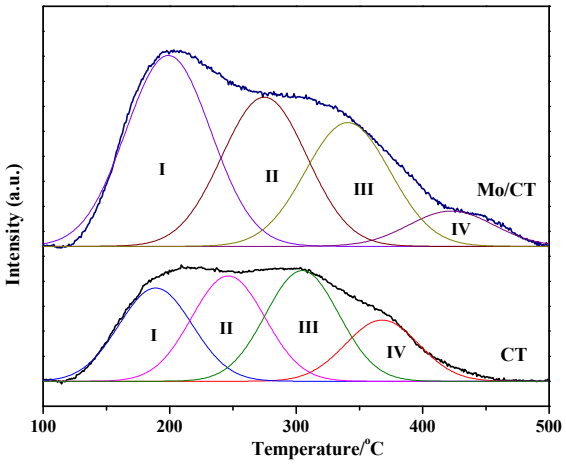


**Fig. 7.** $NH_3$-TPD profiles of the CT and Mo/CT samples.

crucial aspect affecting the catalytic activity apart from the redox property. Accordingly, $NH_3$-TPD and *in situ* $NH_3$ adsorption experiments were employed to evaluate the adsorption behavior of $NH_3$ on the surface of CT and Mo/CT catalysts. First, the $NH_3$-TPD experiment was performed to probe the number of acid sites in the CT and Mo/CT catalysts, and the corresponding results are shown in Fig. 7. It can be seen that the $NH_3$-TPD profiles of CT and Mo/CT catalysts both exhibited four desorption peaks in the temperature range of measurements, which are labeled as I, II, III, and IV. The Peak I around 150 °C was assigned to the desorption of physisorbed $NH_3$ species. Peak II was attributed to weak acid sites, and the peaks III and IV were ascribed to strong acid sites [14,43]. The quantitative analysis results of $NH_3$-TPD are summarized in Table 1. It shows that the total acidity of CT and Mo/CT was 0.49 and 0.68 mg/g, respectively. Evidently, the Mo/CT catalyst exhibited a remarkably increased total acid amount compared with CT, which suggested that Mo surface modification can effectively improve the surface acidity of Mo/CT catalyst to promote the adsorption of $NH_3$ molecules, and finally enhance the $NH_3$-SCR activity.

### 3.3.2. $NH_3$-adsorption in situ DRIFTS

$NH_3$-TPD can determine the total number of acid sites, but it fails to distinguish Brönsted acid sites and Lewis acid sites on catalyst surface. To ascertain the nature of acid sites and acquire more information of the increased acidity, $NH_3$ adsorption *in situ* DRIFTS was carried out, and the corresponding results are depicted in Fig. 8. For the CT catalyst in Fig. 8A, after $NH_3$ adsorption and $N_2$ purge, several bands were detected in the range of 1000–2000 $cm^{-1}$. The bands at 1579 and 1181 $cm^{-1}$ were ascribed to coordinated $NH_3$ bound to Lewis acid sites, and the weak band at 1440 $cm^{-1}$ could be related to the $NH_4^+$ species on Brönsted acid sites [19,28,44]. For the Mo/CT catalyst in Fig. 8B, the *in situ* DRIFT spectra of $NH_3$ adsorption were obviously different from that of the CT catalyst. In addition to the band at 1183 $cm^{-1}$ attributed to the coordinated $NH_3$ linked to Lewis acid sites, a new band at 1672 $cm^{-1}$ assigned to $NH_4^+$ species bound to Brönsted acid sites was observed [18,45,46]. Moreover, the intensity of the band at 1433 $cm^{-1}$ ascribed to the $NH_4^+$ species bound to Brønsted acid sites was much stronger than that of the CT catalyst. With the temperature rising, all bands became weaker and the band intensity of Brönsted acid sites (1440, 1433, 1672 $cm^{-1}$) decreased faster than that of Lewis acid sites. This phenomenon indicated that $NH_3$ bonded to Lewis acid sites was more stable than that bonded to Brönsted acid sites on catalyst surface. Combining with the $NH_3$-TPD results, the weak acid should be related to the Brönsted acid and the strong acid was related to the Lewis acid. This meant that the loading of Mo could result in more Brönsted acid sites on the Mo/CT catalyst surface, and similar results were found on $CeO_2$-$MoO_3$ catalyst in Li's work [35]. Moreover, we can find that the area ratio of Brönsted acid sites to total acid sites over Mo/CT was much higher than that on CT in the low-temperature range (< 300 °C) (Fig. S2). And, Mo/CT displayed the higher NO conversion in the same temperature range (Fig. 1). These phenomena suggested that the larger number of Brönsted acid sites caused by Mo addition played an important role in the improvement of catalytic activity in the low-temperature range over the Mo/CT catalyst for $NH_3$-SCR reaction in the present work.

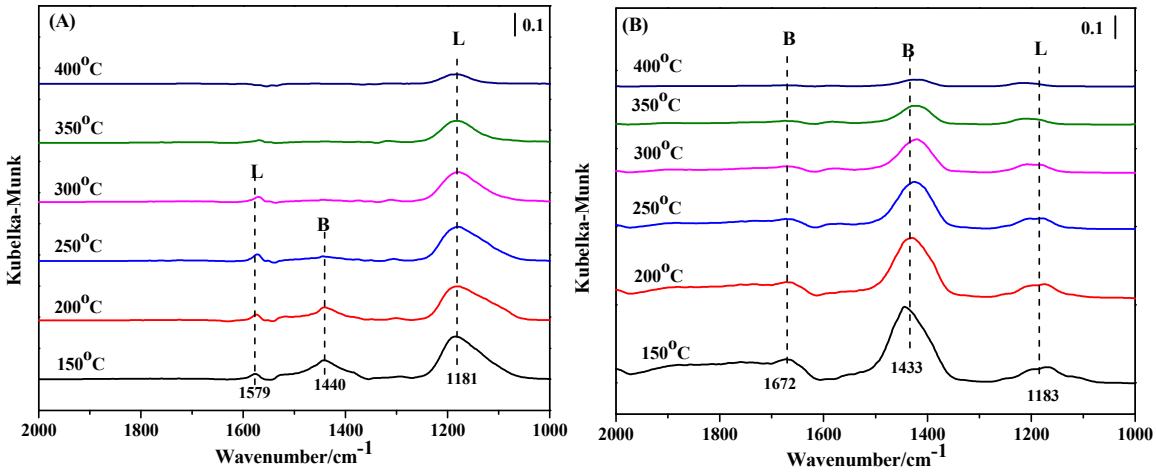


**Fig. 8.** $NH_3$ adsorption *in situ* DRIFTS of (A) CT and (B) Mo/CT catalyst.

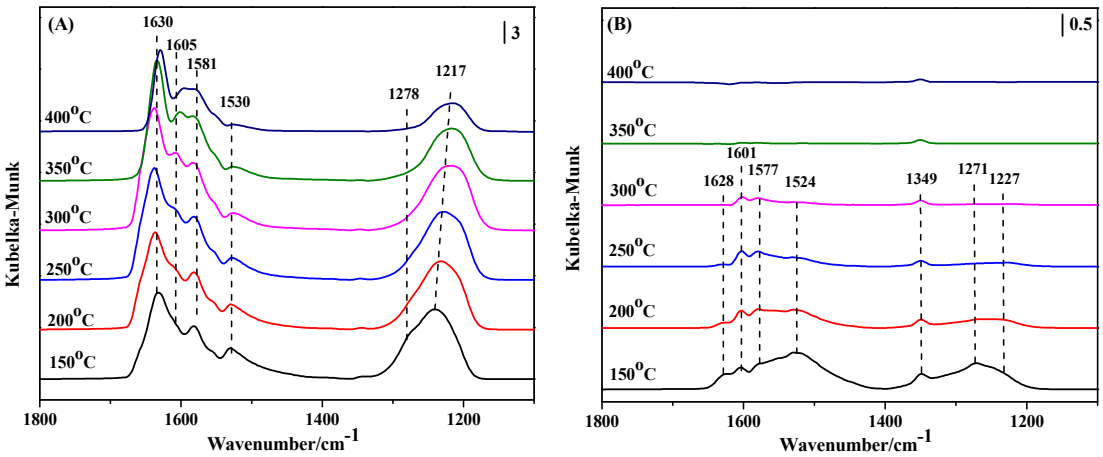


**Fig. 9.** NO + $O_2$ adsorption *in situ* DRIFTS of (A) CT and (B) Mo/CT catalysts.

### 3.3.3. *NO + $O_2$-adsorption in situ DRIFTS*

The *in situ* DRIFT experiments of NO + $O_2$ co-adsorption were also employed to probe the surface adsorption the $NO_x$ species over the two catalysts. For the CT catalyst (Fig. 9A), several vibration bands attributed to adsorbed nitrate species were observed when it was exposed to NO + $O_2$. According to the literature, the band at 1630 $cm^{-1}$ was ascribed to bridging bidentate nitrates, the bands at 1605 and 1217 $cm^{-1}$ were attributed to bridging monodentate nitrates, the band located at 1580 $cm^{-1}$ was assigned to bidentate nitrates, and the bands at 1530 and 1278 $cm^{-1}$ were assigned to monodentate nitrates. For the Mo/CT catalyst (Fig. 9B), when NO + $O_2$ were introduced into the DRIFTS cell at 150 °C, some bands attributed to adsorbed $NO_x$ species were also observed: bridged nitrates (1628, 1601, and 1227 $cm^{-1}$), monodentate nitrates (1524 and 1271 $cm^{-1}$), and bidentate nitrates (1577 $cm^{-1}$) [47–52]. The bands at 1349 $cm^{-1}$ attributed to ionic nitrate also appeared [53–55]. Compared with the NO + $O_2$ spectra of the CT and Mo/CT samples, it is worth noting that the intensity of adsorbed $NO_x$ species on Mo/CT was significantly weaker than that on CT. Moreover, with increasing temperature, the band intensities of adsorbed $NO_x$ species became weaker gradually. Especially, the adsorbed $NO_x$ species on the Mo/CT catalyst disappeared completely at 300 °C. The above results suggested that the highly dispersed molybdenum on Mo/CT not only resulted in more Brönsted acid sites formed on the catalyst surface, but also reduced the thermal stability of the inactive nitrate species, leaving more active sites available for the adsorption of $NH_3$, both of which were favorable for the promotion of SCR activity.

### 3.4. *Interaction with reactants ($NH_3$ + NO + $O_2$ co-adsorption in situ DRIFTS)*

To investigate the reaction mechanism of $NH_3$-SCR reaction over the CT and Mo/CT catalysts, *in situ* DRIFTS of $NH_3$ + NO + $O_2$ co-adsorption was performed, and the results are displayed in Fig. 10. When the CT sample was exposed to the $NH_3$ + NO + $O_2$ mixed gas at room temperature, bidentate nitrate (1563 $cm^{-1}$), monodentate nitrate (1520 and 1278 $cm^{-1}$), and bridging nitrate (1624 and 1228 $cm^{-1}$) were observed over the catalyst. Furthermore, combining the results of $NH_3$ adsorption *in situ* DRIFTS, the band at 1444 $cm^{-1}$ related to $NH_4^+$ ions bonded on Brönsted acid sites was also detected. Along with the rise of temperature, the band of Brönsted acid sites disappeared at

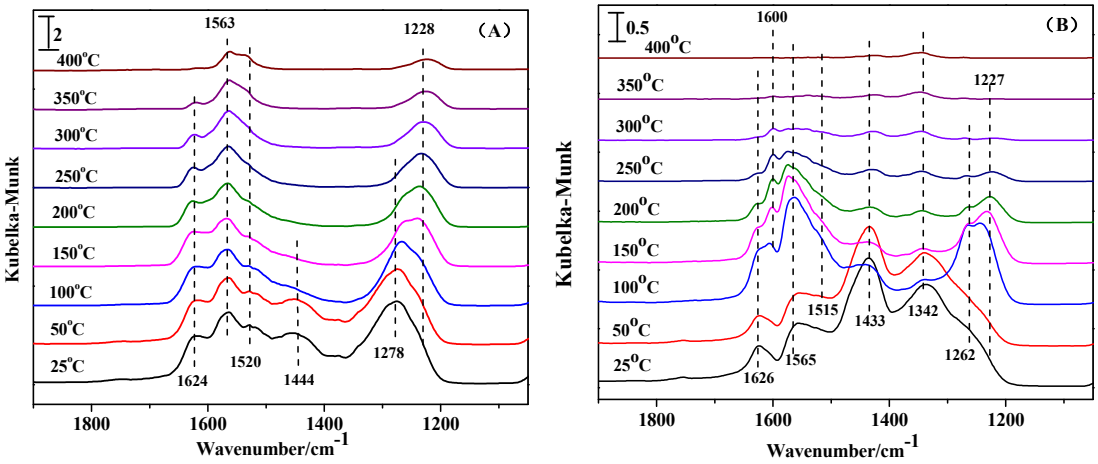


**Fig. 10.** $NH_3$ + NO + $O_2$ adsorption *in situ* DRIFTS of (A) CT and (B) Mo/CT catalysts.

200 °C due to the desorption of $NH_3$ and the reaction between the adsorbed $NH_3$ species and $NO_x$ species. More importantly, some interesting phenomena about adsorbed $NO_x$ species were observed during the heating process. The band of monodentate nitrate (1278 $cm^{-1}$) disappeared at 200 °C because of its poor thermal stability, and the band intensity of bidentate nitrate (1563 $cm^{-1}$) and bridging nitrate (1624 and 1228 $cm^{-1}$) increased with increasing temperature first and then decreased with a further increase in temperature, which was related to the reaction between the adsorbed $NO_x$ and $NH_3$ species, as well as the transformation and dissociation of the adsorbed $NO_x$ species. However, these bidentate and bridging nitrates did not disappear even at 400 °C owing to the strong adsorption. With regard to the Mo/CT catalyst, the bands of bridging nitrate (1626 and 1227 $cm^{-1}$), bidentate nitrate (1600 and 1565 $cm^{-1}$), monodentate nitrate (1515 and 1262 $cm^{-1}$), and Brönsted acid (1433 $cm^{-1}$) were also detected at corresponding positions. And the variation of these bands was similar to that of the CT catalyst with an increase in temperature. More significantly, however, a new band at 1342 $cm^{-1}$ was observed, which was attributed to the intermediate species generated by the reaction of the adsorbed $NH_3$ and $NO_x$ species [56]. This may be one reason that the Mo/CT catalyst displayed better catalytic performance than the CT catalyst for $NH_3$-SCR reaction.

## 4. Conclusions

A novel Mo-promoted $CeO_2$-$TiO_2$ catalyst has been developed for the selective catalytic reduction of NO by $NH_3$, which showed high de$NO_x$ efficiency from 150 to 400 °C. The redox properties and surface acidity of the $MoO_3$/$CeO_2$-$TiO_2$ catalyst were affected markedly by the addition of Mo species, thereby modified the adsorption of $NH_3$ and $NO_x$ on the catalyst surface. The improvement of SCR activity over $MoO_3$/$CeO_2$-$TiO_2$ may be directly correlated to the increase in the number of Brönsted acid sites and weakly adsorbed $NO_x$ species, as opposed to a decrease in the BET surface area and a change in the redox properties. Our results can provide a scientific reference for the development of $CeO_2$-based catalysts for practical applications.

## References


[1] C. X. Li, M. Q. Shen, J. Q. Wang, J. Wang, Y. P. Zhai, *Ind. Eng. Chem. Res.*, **2018**, 57, 8424–8435.
[2] J. K. Lai, I. E. Wachs, *ACS Catal.*, **2018**, 8, 6537–6551.
[3] T. F. Xu, X. D. Wu, Y. X. Gao, Q. W. Lin, J. F. Hu, D. Weng, *Catal. Commun.*, **2017**, 93, 33–36.
[4] T. H. Vuong, J. Radnik, J. Rabeah, U. Bentrup, M. Schneider, H. Atia, U. Armbruster, W. Grünert, A. Brückner, *ACS Catal.*, **2017**, 7, 1693–1705.
[5] I. Song, S. Youn, H. Lee, S. G. Lee, S. J. Cho, D. H. Kim, *Appl. Catal. B*, **2017**, 210, 421–431.
[6] G. Gao, J. W. Shi, C. Liu, C. Gao, Z. Y. Fan, C. M. Niu, *Appl. Surf. Sci.*, **2017**, 411, 338–346.
[7] C. Liu, G. Gao, J. W. Shi, C. He, G. D. Li, N. Bai, C. M. Niu, *Catal. Commun.*, **2016**, 86, 36–40.
[8] Z. Y. Sheng, D. R. Ma, D. Q. Yu, X. Xiao, B. J. Huang, L. Yang, S. Wang, *Chin. J. Catal.*, **2018**, 39, 821–830.
[9] W. Li, C. Zhang, X. Li, P. Tan, A. L. Zhou, Q. Y. Fang, G. Chen, *Chin. J. Catal.*, **2018**, 39, 1653–1663.


### Graphical Abstract

*Chin. J. Catal.*, 2020, 41: 364–373 doi: S1872-2067(19)63437-6

**Enhanced low-temperature $NH_3$-SCR performance of $CeTiO_x$ catalyst via surface Mo modification**

Lulu Li, Peixiao Li, Wei Tan, Kaili Ma, Weixin Zou, Changjin Tang *, Lin Dong *
*Nanjing University;*
*Emergency Center for Environmental Monitoring at Canal Head of Middle Route of South-to-North Water Transfer Project*

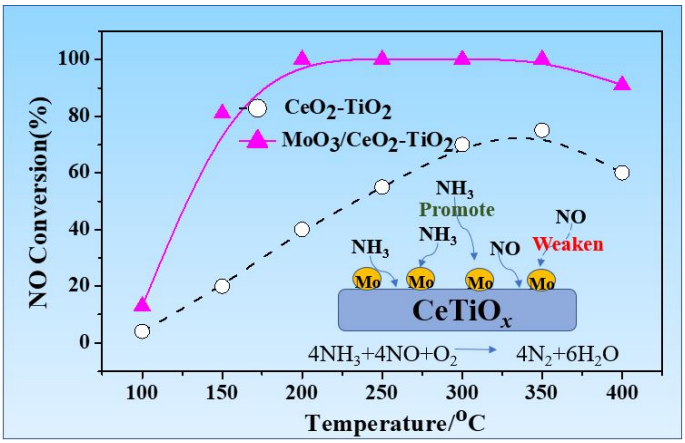


Mo surface modification improves the low-temperature $NH_3$-SCR activity and $SO_2$-poisoning resistance of the $CeTiO_x$ catalyst because the acid site number is significantly increased and the adsorption of nitrate species is weakened.

[10] S. Zhang, S. J. Liu, W. S. Hu, X. B. Zhu, R. Y. Qu, W. H. Wu, C. H. Zheng, X. Gao, *Appl. Surf. Sci*., **2019**, 466, 99–109.
[11] L. Kang, L. Han, J. He, H. Li, T. Yan, G. Chen, J. Zhang, L. Shi, D. Zhang, *Environ. Sci. Technol*., **2019**, 53, 938–945.
[12] L. Han, M. Gao, C. Feng, L. Shi, D. Zhang, *Environ. Sci. Technol*., **2019**, 53, 5946–5956.
[13] L. Han, M. Gao, J. Y. Hasegawa, S. Li, Y. Shen, H. Li, L. Shi, D. Zhang, *Environ. Sci. Technol*., **2019**, 53, 6462–6473.
[14] L. Zhang, L. L. Li, Y. Cao, Y. Xiong, S. G. Wu, J. F. Sun, C. J. Tang, F. Gao, L. Dong, *Catal Sci. Technol*., **2015**, 5, 2188–2196.
[15] D. W. Kwon, S. C. Hong, *Appl. Surf. Sci*., **2015**, 356, 181–190.
[16] X. L. Li, Y. H. Li, S. S. Deng, T. A. Rong, *Catal. Commun*., **2013**, 40, 47–50.
[17] W. Q. Xu, Y. B. Yu, C. B. Zhang, H. He, *Catal. Commun*., **2008**, 9, 1453–1457.
[18] X. Gao, Y. Jiang, Y. C. Fu, Y. Zhong, Z. Y. Luo, K. F. Cen, *Catal. Commun*., **2010**, 11, 465–469.
[19] Z. Liu, J. Zhu, J. Li, L. Ma, S. I. Woo, *ACS Appl. Mater. Interfaces*, **2014**, 6, 14500–14508.
[20] W. P. Shan, F. D. Liu, H. He, X. Y. Shi, C. B. Zhang, *Appl. Catal. B*, **2012**, 115–116, 100–106.
[21] X. Gao, X. S. Du, L. W. Cui, Y. C. Fu, Z. Y. Luo, K. F. Cen, *Catal. Commun*., **2010**, 12, 255–258.
[22] M. E. Yu, C. T. Li, G. M. Zeng, Y. Zhou, X. N. Zhang, Y. E. Xie, *Appl. Surf. Sci*., **2015**, 342, 174–182.
[23] Z. M. Liu, Y. X. Liu, B. H. Chen, T. L. Zhu, L. L. Ma, *Catal. Sci. Technol*., **2016**, 6, 6688–6696.
[24] Y. Qiu, B. Liu, J. Du, Q. Tang, Z. H. Liu, R. L. Liu, C. Y. Tao, *Chem. Eng. J*., **2016**, 294, 264–272.
[25] Y. Jiang, Z. M. Xing, X. C. Wang, S. B. Huang, Q. Y. Liu, J. S. Yang, *J. Ind. Eng. Chem*., **2015**, 29, 43–47.
[26] L. L. Li, W. Tan, X. Q. Wei, Z. X. Fan, A. N. Liu, K. Guo, K. L. Ma, S. H. Yu, C. Y. Ge, C. J. Tang, L. Dong, *Catal. Commun*., **2018**, 114, 10–14.
[27] X. Li, X. Li, J. Li, J. Hao, *J. Hazard. Mater*., **2016**, 318, 615–622.
[28] Z. M. Liu, S. X. Zhang, J. H. Li, L. L. Ma, *Appl. Catal. B*, **2014**, 144, 90–95.
[29] Z. Y. Fei, Y. R. Yang, M. H. Wang, Z. L. Tao, Q. Liu, X. Chen, M. F. Cui, Z. X. Zhang, J. H. Tang, X. Qiao, *Chem. Eng. J*., **2018**, 353, 930–939.
[30] Z. M. Liu, H. Su, J. H. Li, Y. Li, *Catal. Commun*., **2015**, 65, 51–54.
[31] W. Yu, J. Zhu, L. Qi, C. Sun, F. Gao, L. Dong, Y. Chen, *J. Colloid Interfaces Sci*., **2011**, 364, 435–442.
[32] J. Zhu, F. Gao, L. H. Dong, W. J. Yu, L. Qi, Z. Wang, L. Dong, Y. Chen, *Appl. Catal. B*, **2010**, 95, 144–152.
[33] X. J. Yao, T. T. Kong, L. Chen, S. M. Ding, F. M. Yang, L. Dong, *Appl. Surf. Sci*., **2017**, 420, 407–415.
[34] X. J. Yao, K. L. Ma, W. X. Zou, S. G. He, J. B. An, F. M. Yang, L. Dong, *Chin. J. Catal*., **2017**, 38, 146–159.
[35] Y. Peng, R. Qu, X. Zhang, J. Li, *Chem. Commun*., **2013**, 49, 6215–6217.
[36] X. L. Hu, Q. Shi, H. Zhang, P. F. Wang, S. H. Zhan, Y. Li, *Catal. Today*, **2017**, 297, 17–26.
[37] X. X. Wang, Y. Shi, S. J. Li, W. Li, *Appl. Catal. B*, **2018**, 220, 234–250.
[38] Y. R. Yang, M. H. Wang, Z. L. Tao, Q. Liu, Z. Y. Fei, X. Chen, Z. X. Zhang, J. H. Tang, M. F. Cui, X. Qiao, *Catal. Sci. Technol*., **2018**, 8, 6396–6406.
[39] H. Liu, Z. X. Fan, C. Z. Sun, *Appl. Catal. B*, **2019**, 244, 671–683
[40] X. J. Yao, R. D. Zhao, L. Chen, J. Du, C. Y. Tao, F. M. Yang, L. Dong, *Appl. Catal. B*, **2017**, 208, 82–93.
[41] Y. Li, Y. Wan, Y. P. Li, S. H. Zhan, Q. X. Guan, Y. Tian, *Appl. Catal. A*, **2016**, 528, 150–160.
[42] Z. L. Wu, A. J. Rondinone, L. N. Ivanov, S. H. Overbury, *J. Phys. Chem. C*, **2011**, 115, 25368–25378.
[43] Y. Xiong, C. J. Tang, X. J. Yao, L. Zhang, L. L. Li, X. B. Wang, Y. Deng, F. Gao, L. Dong, *Appl. Catal. A*, **2015**, 495, 206–216.
[44] K. Liu, F. D. Liu, L. J. Xie, W. P. Shan, H. He, *Catal. Sci. Technol*., **2015**, 5, 2290–2299.
[45] Y. Peng, K. Z. Li, J. H. Li, *Appl. Catal. B*, **2013**, 140–141, 483–492.
[46] S. M. Lee, K. H. Park, S. C. Hong, *Chem. Eng. J*., **2012**, 195–196, 323–331.
[47] X. M. Wang, X. Y. Li, Q. D. Zhao, W. B. Sun, M. Tade, S. M. Liu, *Chem. Eng. J*., **2016**, 288, 216–222.
[48] X. J. Yao, L. Chen, J. Cao, F. M. Yang, W. Tan, L. Dong, *Ind. Eng. Chem. Res*., **2018**, 57, 12407–12419.
[49] F. D. Liu, H. He, *Catal. Today*, **2010**, 153, 70–76.
[50] T. Zhang, R. Y. Qu, W. K. Su, J. H. Li, *Appl. Catal. B*, **2015**, 176–177, 338–346.
[51] W. Shan, F. Liu, H. He, X. Shi, C. Zhang, *Chem. Commun*., **2011**, 47, 8046–8048.
[52] X. L. Li, Y. H. Li, *J. Mol. Catal. A*, **2014**, 386, 69–77.
[53] K. B. Nam, D. W. Kwon, S. C. Hong, *Appl. Catal. A*, **2017**, 542, 55–62.
[54] J. Liu, X. Y. Li, Q. D. Zhao, J. Ke, H. N. Xiao, X. J. Lv, S. M. Liu, M. Tadé, S. B. Wang, *Appl. Catal. B*, **2017**, 200, 297–308.
[55] S. P. Ding, F. D. Liu, X. Y. Shi, K. Liu, Z. H. Lian, L. J. Xie, H. He, *ACS Appl. Mater. Interfaces*, **2015**, 7, 9497–9506.
[56] Z. R. Ma, X. D. Wu, Z. C. Si, D. Weng, J. Ma, T. F. Xu, *Appl. Catal. B*, **2015**, 179, 380–394.

# 表面Mo修饰提高$CeTiO_x$催化剂低温脱硝性能

李露露[a,c], 李佩晓[d], 谭　伟[b], 马凯莉[b], 邹伟欣[b], 汤常金[b,c,#], 董　林[a,c,*]

[a]南京大学环境学院, 江苏南京210093
[b]南京大学化学化工学院, 江苏南京210093
[c]南京大学现代分析中心, 江苏省机动车尾气污染控制重点实验室, 江苏南京210093
[d]南水北调中线渠首环境检测应急中心, 河南南阳473061

**摘要**: 近年来, 以雾霾为代表的大气污染问题严重影响到经济社会的可持续发展. 其中, 氮氧化物($NO_x$)的大量排放是导致雾霾天气的重要原因之一. 氨选择性催化还原($NH_3$-SCR)是目前消除氮氧化物的主流技术, 低温$NH_3$-SCR更是广泛应用于钢铁、焦化、水泥、玻璃、陶瓷和垃圾焚烧等行业的烟气排放治理. 传统的$V_2O_5$-$WO_3$/$TiO_2$催化剂活性温度高(300–400 °C)且钒具有生物毒性, 因此亟待开发环境友好的低温非钒基脱硝催化剂.

最近, $CeTiO_x$基催化剂由于在中高温段(250–400 °C)表现出优异的脱硝性能而得到广泛关注. 然而, 该催化剂仍面临低温活性差及抗硫性能差的问题, 制约了其工业化应用. 研究显示, 添加过渡金属可提高$CeTiO_x$基催化剂的脱硝活性和抗硫

中毒性能, 这主要是因为过渡金属的添加可以有效改善催化剂的氧化还原性能和表面酸性. $MoO_3$作为一种可以提供大量酸性位的氧化物, 常被用作助剂改善钒钨钛催化剂的活性. 研究显示, $MoO_3$的引入可以促进催化剂中钒物种的分散度以及提高表面酸性. 基于此, 我们制备了一系列不同Mo含量的$MoO_3$/$CeTiO_x$催化剂, 以期提高$CeTiO_x$催化剂的低温脱硝性能及抗$SO_2$中毒能力, 并着重研究表面Mo的修饰对$CeTiO_x$催化剂物理化学性质的影响.

研究发现, 表面Mo修饰可以显著提高$CeTiO_x$的低温催化活性, 其脱硝效率在150 °C即可达到80%, 同时抗$SO_2$中毒能力也得到增强. 进一步借助X射线衍射、比表面积测定、氢气程序升温还原、氨气程序升温脱附和X射线光电子能谱等方法对催化剂进行了全面表征分析. 结果显示, 表面Mo修饰对$CeTiO_x$催化剂物理化学性质的影响与其脱硝性能有着密不可分的关系. 首先, 钼物种主要是以$MoO_3$的形式存在于$CeTiO_x$表面, 其最佳的负载量为4 wt.%. 其次, 表面Mo的沉积显著提高了催化剂的表面酸量, 尤其是Brönsted酸位的数量, 而表面酸位的增加有利于催化剂吸附与活化反应物种$NH_3$; 同时, 表面Mo修饰还减弱了硝酸盐在催化剂表面的吸附, 进一步促使$NH_3$-SCR反应按照Eley-Rideal机理顺利进行. 最后, 该催化剂在$H_2O$和$SO_2$存在的条件下仍具有最佳的脱硝性能, 因而有望用于实际含$SO_2$的低温烟气脱硝.

**关键词**: 氮氧化物消除; 氧化铈-氧化钛催化剂; 氧化钼表面修饰; 二氧化硫中毒; 表面酸性

收稿日期: 2019-05-20. 接受日期: 2019-07-05. 出版日期: 2020-02-05.

*通讯联系人. 电话: (025)83592290; 传真: (025)83317761; 电子信箱: donglin@nju.edu.cn

#通讯联系人. 电子信箱: tangcj@nju.edu.cn

基金来源: 国家自然科学基金(21773106, 21707066, 21677069, 21806077)和中国博士后科学基金(2018M642206).

本文的电子版全文由Elsevier出版社在ScienceDirect上出版(http://www.sciencedirect.com/science/journal/18722067).